

THE IMPACT OF GAS BULK ROTATION ON THE LYMAN α LINE

JUAN N. GARAVITO-CAMARGO, JAIME E. FORERO-ROMERO

Departamento de Física, Universidad de los Andes, Cra. 1 No. 18A-10, Edificio Ip, Bogotá, Colombia

AND

MARK DIJKSTRA

Institute of Theoretical Astrophysics, University of Oslo, Postboks 1029, 0858 Oslo, Norway

Submitted for publication in ApJ

ABSTRACT

We present results of radiative transfer calculations to measure the impact of gas bulk rotation on the morphology of the Lyman α emission line in distant galaxies. We model a galaxy as a sphere with an homogeneous mixture of dust and hydrogen at a constant temperature. These spheres have a solid-body rotation with maximum velocities in the range $0 - 300 \text{ km s}^{-1}$ and neutral hydrogen optical depths in the range $\tau_{\text{H}} = 10^5 - 10^7$. We consider cases of a single central Lyman α source, and a uniform distribution of sources. Our main result is that rotation introduces a dependence of the line morphology with viewing angle. Observations parallel to the rotation axis yield lines similar to the static case. The greatest difference is observed perpendicular to the rotation axis where the intensity at the line center increases with rotational velocity. For homogeneously distributed sources the line becomes single peaked at rotational velocities larger than half the line width in the static case. However, rotation does not induce any significant anisotropy in the total line intensity or in the escape fraction.

Subject headings: galaxies: high-redshift — line: formation — methods: numerical — radiative transfer

1. INTRODUCTION

The detection of strong Ly α emission lines has become an essential method in extra-galactic astronomy to find distant star-forming galaxies (Partridge & Peebles 1967; Rhoads et al. 2000; Gawiser et al. 2007; Koehler et al. 2007; Ouchi et al. 2008; Yamada et al. 2012; Schenker et al. 2012; Finkelstein et al. 2013). The galaxies detected using this method receive the name of Ly α emitters (LAEs). A detailed examination of this galaxy population has diverse implications for galaxy formation, reionization and the large scale structure of the Universe. Attempts to fully exploit the physical information included in the Ly α line require an understanding of all the physical factors involved in shaping the line. Due to the resonant nature of this line, these physical factors notably include temperature, density and bulk velocity field of the neutral Hydrogen in the emitting galaxy and its surroundings.

A basic understanding of the quantitative behavior of the Ly α line has been reached through analytic studies in the case of a static configurations, such as uniform slabs (Adams 1972; Harrington 1973; Neufeld 1990) and uniform spheres (Dijkstra et al. 2006). Analytic studies of configurations including some kind of bulk flow only include the case of a sphere with a Hubble like expansion flow (Loeb & Rybicki 1999).

A quantitative description of the Ly α line has been reached through Monte Carlo simulations (Auer 1968; Avery & House 1968; Adams 1972). In the last two decades these studies have become popular due to the availability of computing power. Early into the 21st century, the first studies focused on homogeneous and static

media (Ahn et al. 2000, 2001; Zheng & Miralda-Escudé 2002). Later on, the effects of clumpy media (Hansen & Oh 2006) and expanding/contracting shell/spherical geometries started to be studied (Verhamme et al. 2006; Dijkstra et al. 2006; Ahn et al. 2014). Similar codes have applied these results to semi-analytic models of galaxy formation (Orsi et al. 2012; Garel et al. 2012) and results of large hydrodynamic simulations (Forero-Romero et al. 2011, 2012; Behrens & Niemeyer 2013). Recently, Monte Carlo codes have also been applied to the results of high resolution hydrodynamic simulations of individual galaxies (Laursen et al. 2009; Barnes et al. 2011; Verhamme et al. 2012; Yajima et al. 2012). Meanwhile, recent developments have been focused on the systematic study of clumpy outflows (Dijkstra & Kramer 2012) and anisotropic velocity configurations (Zheng & Wallace 2013).

The recent studies of galaxies in hydrodynamic simulations (Laursen et al. 2009; Barnes et al. 2011; Verhamme et al. 2012; Yajima et al. 2012) have all shown systematic variations in the Ly α line with the viewing angle. These variations are a complex superposition of anisotropic density configurations (i.e. edge-on vs. face-on view of a galaxy), the inflows observed by gas cooling and the outflows included in the supernova feedback process of the simulation. These bulk flows physically correspond to the circumgalactic and intergalactic medium (CGM and IGM). These effects are starting to be studied in simplified configurations that vary the density and wind characteristics (Zheng & Wallace 2013; Behrens et al. 2014).

However, in all these efforts the effect of rotation, which is an ubiquitous feature in galaxies, has not been systematically studied. The processing of the Ly α photons in a rotating interstellar medium (ISM) must have

some kind of impact in the Ly α line morphology.

Performing that study is the main goal of this paper. We investigate for the first time the impact of rotation on the morphology of the Ly α line. We focus on a simplified system: a spherical gas cloud with homogeneous density and solid body rotation, to study the line morphology and the escape fraction in the presence of dust. We base our work on two independent Monte Carlo based radiative transfer codes presented in Forero-Romero et al. (2011) and Dijkstra & Kramer (2012).

This paper is structured as follows: In §2 we present the implementation of bulk rotation into the Monte Carlo codes, paying special attention to coordinate definitions. We also present a short review of how the Ly α radiative transfer codes work and list the different physical parameters in the simulated grid of models. In §3 we present the results of the simulations, with special detail to quantities that show a clear evolution as a function of the sphere rotational velocity. In §4 we discuss the implications of our results in the interpretation of LAEs observations with high resolution spectroscopy. In the last section we present our conclusions.

In this paper we express a photon's frequency in terms of the dimensionless variable $x \equiv (\nu - \nu_a)/\Delta\nu_\alpha$, where $\nu_\alpha = 2.46 \times 10^{15}$ Hz is the Ly α resonance frequency, $\Delta\nu_\alpha \equiv \nu_\alpha \sqrt{2kT/m_p c^2} \equiv \nu_\alpha v_{th}/c$ is the Doppler broadening of the line which depends on the neutral gas temperature T scattering the radiation or equivalently the thermal velocity v_{th} of the atoms. For the temperature $T = 10^4$ K used in our radiative transfer calculations the thermal velocity is $v_{th} = 12.8$ km s $^{-1}$.

2. MODELS OF BULK GAS ROTATION

Describing the kinematics of gas rotation in all generality is a complex task, specially at high redshift where there is still missing a thorough observational account of rotation in galaxies beyond $z > 1.0$. Even at low redshifts there is a great variation in the shape of the rotation curve as observed in HI emission as a function of the distance to the galaxy center. However there are two recurrent features. First, in the central galactic region the velocity increases proportional to the radius, following a solid rotation behavior. Second, beyond a certain radius the rotation curve tends to flatten. An ab-initio description of such realistic rotation curves in simulations depends on having access to the dynamic evolution of all mass components in the galaxy: stars, gas and dark matter. Such level of realism is extremely complex to achieve, specially if one wants to get a systematic description based on statistics of simulated objects.

Following the tradition of studies of Ly α emitting systems, we implement a model with simplified geometry. We assume that the gas is homogeneously distributed in a sphere that rotates as a solid body with constant angular velocity. This simple model will contain only one free parameter: the linear velocity at the sphere's surface, V_{max} .

2.1. Detailed Implementation of Rotation

In the Monte Carlo code we define a Cartesian coordinate system to describe the position of each photon. The origin of this system coincides with the center of the sphere and the rotation axis is defined to be z-axis. With

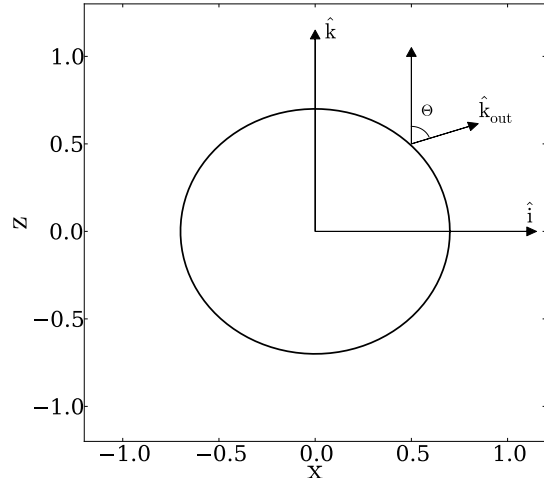


FIG. 1.— Geometry of the gas distribution. The angular velocity vector is parallel to the unit vector \hat{k} . In order to describe the departures from spherical symmetry we use the polar angle θ formed by the direction of the outgoing photons with respect to the z-axis. We define the variable $\mu \equiv \cos \theta$ to report to present our results.

this choice, the components of the gas bulk velocity field, $\vec{v} = v_x \hat{i} + v_y \hat{j} + v_z \hat{k}$, can be written as

$$v_x = -\frac{y}{R} V_{max}, \quad (1)$$

$$v_y = \frac{x}{R} V_{max}, \quad (2)$$

$$v_z = 0, \quad (3)$$

where R is the radius of the sphere and V_{max} is the linear velocity at the sphere's surface. The minus/plus sign in the x/y -component of the velocity indicates the direction of rotation. In this case we take the angular velocity in the same direction as the \hat{k} unit vector. With these definitions we can write the norm of the angular velocity as $\omega = V_{max}/R$.

For each photon in the simulation we have its initial position inside the sphere, direction of propagation \hat{k}_{in} and reduced frequency x_{in} . The photon's propagation stops once they cross the surface of the sphere. At this point we store the position, the outgoing direction of propagation \hat{k}_{out} and the reduced frequency x_{out} . We now define the angle θ by $\cos \theta = \hat{k}_{out} \cdot \hat{k} \equiv \mu$, it is the angle of the outgoing photons with respect to the direction of the angular velocity. We use the variable μ to study the anisotropy induced by rotation. Figure 1 shows the geometry of the problem and the important variables.

2.2. Brief Description of the Radiative Transfer Codes

Here we briefly describe the relevant points for the two radiative transfer codes we have used. For a detailed description we refer the reader to the original papers Forero-Romero et al. (2011); Dijkstra & Kramer (2012).

The codes follow the individual scatterings of Ly α photons as they travel through a 3D distribution of neutral Hydrogen. At each scattering the frequency of the photon (in the laboratory frame) and its direction of propagation change. This change in frequency is due to the

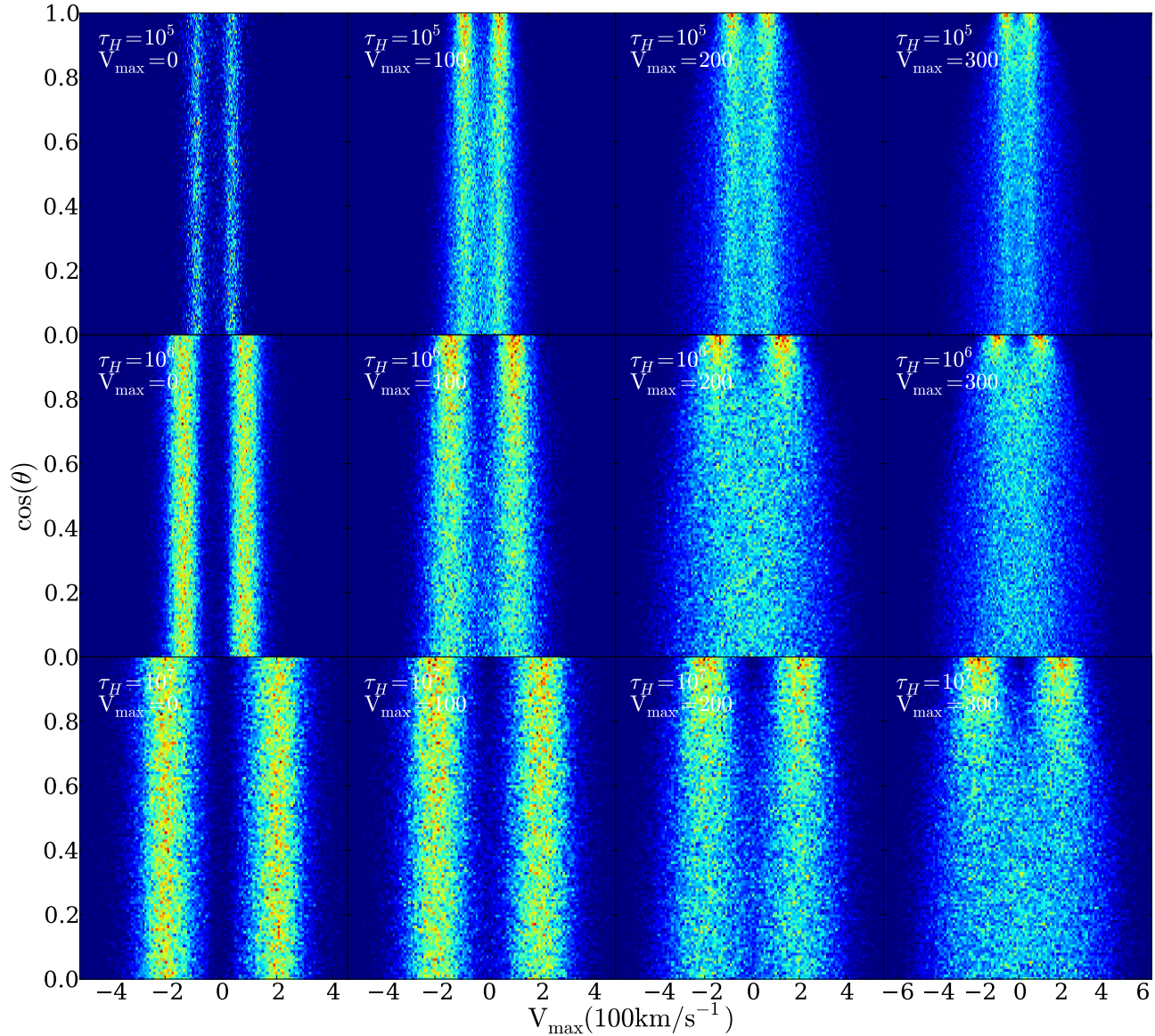


FIG. 2.— 2D histogram showing the number of photons that escape with frequency x forming an angle θ (parameterized as $\cos\theta$) with the rotation axis. The rotational velocity (0, 100, 200, 300 km s^{-1}) increases from left to right and the optical depth (10^5 , 10^6 , 10^7) from top to bottom. The Ly α photons are initialized at the center of the sphere.

peculiar velocities of the Hydrogen atom that absorbed and re-emitted the photon. If dust is present, the photon can interact either with a Hydrogen atom or dust grain. In the case of a dust interaction the photon can be either absorbed or scattered, this probability is encoded in the dust albedo, A , which we chose to be 1/2. In order to obtain accurate values for the escape fraction of photons in the presence of dust, we do not use any accelerating mechanism in the radiative transfer. Once the photons escape the gas distribution we store their direction at their direction of propagation and frequency at their last scattering.

The photons are thus emitted in some region of the gas distribution and follow a random walk in space and frequency until they escape the gas distribution or are absorbed by a dust grain. The initialization process for the Ly α photons has to specify its position, frequency

and direction of propagation. In our case we select the initial frequency to be exactly the Ly α rest-frame frequency ($x = 0$) and the direction of propagation to be random following a flat probability distribution over the sphere. A different initialization that uses a Gaussian with a velocity with equal to the thermal velocity, 12.8 km s^{-1} in our case, should not introduce noticeable change given that our rotational velocities span the range $100\text{--}300 \text{ km s}^{-1}$ and the lines have velocity widths on the order of $100\text{--}500 \text{ km s}^{-1}$.

The gas is completely defined by its geometry (i.e. sphere or slab), temperature T , Hydrogen optical depth τ_H , dust optical depth τ_a and the bulk velocity field \vec{v} . Our codes treat the gas as homogeneous in density (τ_H , τ_a) and temperature.

2.3. Grid of Simulated Galaxies

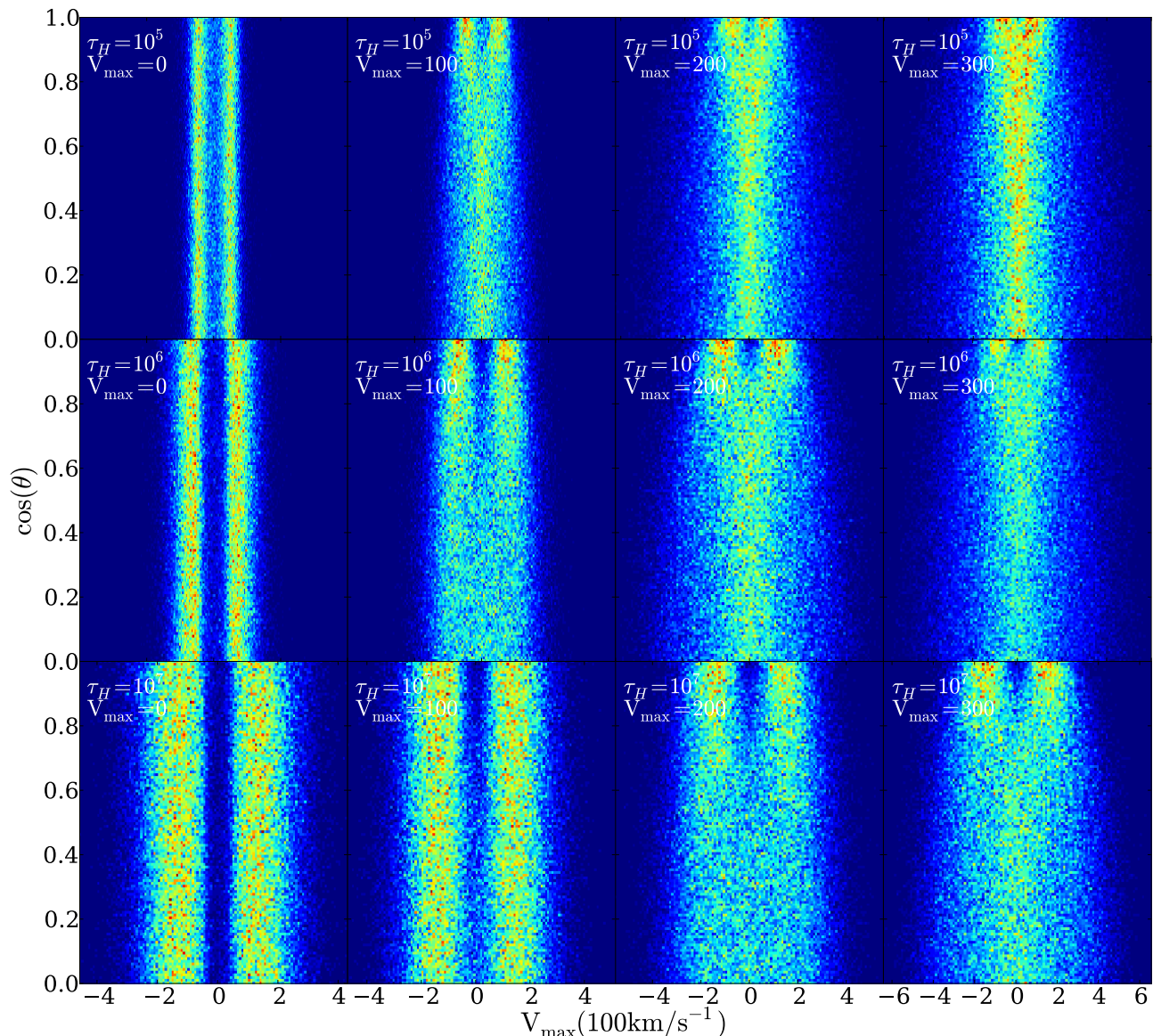


FIG. 3.— Same as Figure 2 for Ly α photons initialized homogeneously throughout the sphere.

In the Monte Carlo calculations we follow the propagation of $N_\gamma = 10^5$ numerical photons through different spherical galaxies. For each galaxy we vary at least one of the following parameters: the maximum rotational velocity V_{\max} , the hydrogen optical depth τ_H , the dust optical depth τ_a and the initial distribution of photons with respect to the gas. There are 60 models initial combining all variations of the input parameters. Table 1 summarizes the different parameters.

Additionally, we have used two independently developed Monte Carlo codes (Forero-Romero et al. 2011; Dijkstra & Kramer 2012) to perform the calculations. The results we report are robust in the sense that they are obtained by both codes.

3. RESULTS

The central results of this paper are summarized in Figures 2 and 3. They show 2D histograms of the escape frequency x and outgoing angle θ parameterized by

Physical Parameter (units)	Symbol	Values
Velocity (km s^{-1})	V_{\max}	0, 50, 100, 200, 300
Hydrogen Optical Depth	τ_H	$10^5, 10^6, 10^7$
Dust Optical Depth	τ_a	0,1
Photons Distributions		Central, Homogeneous

TABLE 1
SUMMARY OF PHYSICAL PARAMETERS OF OUR MONTE CARLO SIMULATIONS.

$|\mu|$. Constructing the emission line with photons around a value of μ would gives us the emission detected by an observer located at an angle θ with respect to the rotation axis. We have verified that the solutions are indeed symmetric with respect to $\mu = 0$.

From these Figures we can see that the line properties change with rotational velocity and depend on the viewing angle θ . In the next subsections we describe in detail the changes of the morphology with velocity, op-

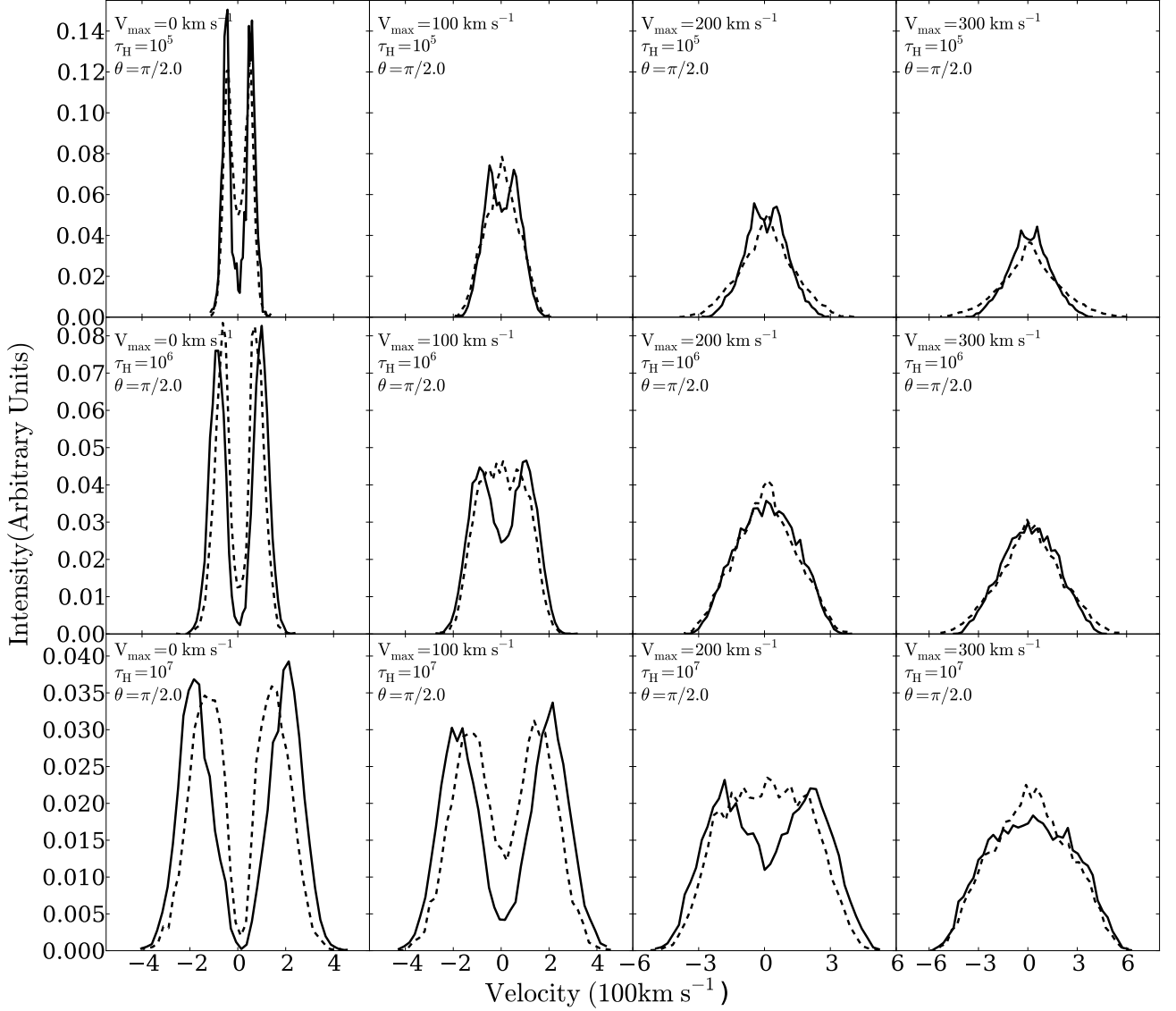


FIG. 4.— Shape of the Ly α line for different maximum rotational velocities for a viewing angle perpendicular to the rotation axis ($|\mu| \sim 0$). The continuous (dashed) line represents the central (homogeneous) source distributions. The panels follow the same correspondence as Figures 2 and 3.

tical depth and viewing angle. We characterize the line morphology by its total intensity, the full width at half maximum (FWHM) and the location of the peak maxima. In order to interpret the morphological changes in the line we also report the median number of scatter for each Ly α photon in the simulation. For the models where dust is included we measure the escape fraction as a function of rotational velocity.

3.1. Line Morphology

The first column in both Figures 2 and 3 shows that for the static sphere the line properties are independent of $|\mu|$, as it is expected due to the spherical symmetry. However, for increasing rotational velocities, at a fixed optical depth, there are clear signs that this symmetry is broken.

If the viewing angle is aligned with the rotation axis, $|\mu| \sim 1$, the Ly α line keeps a double peak with some changes as a function of the rotational velocity that are

easier to spot in models where the Ly α photons are homogeneously distributed than in the case of central emission.

However, for a line of sight perpendicular to the rotation axis, $|\mu| \sim 0$, the impact of rotation is larger. This is clear in Figure 4 where we present the different line morphologies for $|\mu| \sim 0$ for both the homogeneous and central configurations. The panels have the same distribution as Figures 2 and 3.

For this case of $|\mu| \sim 0$, there are three clear effects on the line's morphology as the rotational velocity increases. First, the line broadens; second, the double peaks reduce their intensity; and third, the intensity at the line center rises. The last two effects merge to give the impression that the double peaks are merged into one at high rotational velocities, a result that is evident for the homogeneously distributed sources as shown in the dashed lines of Figure 4.

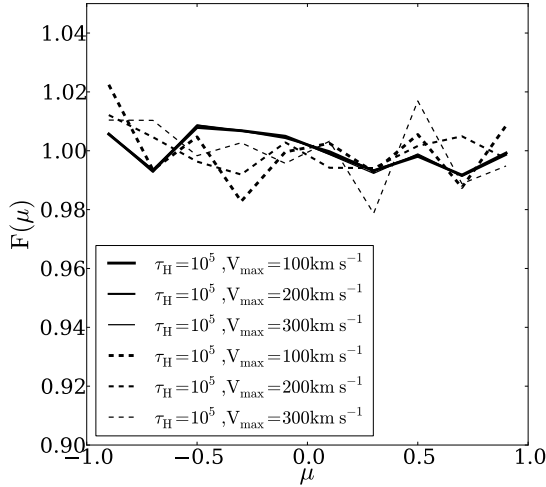


FIG. 5.— Integrated flux distribution, $F(\mu)$, as a function of the viewing angle as parameterized by μ . We show the results for the homogeneous source distribution in models with rotational velocities 0 km s^{-1} , 300 km s^{-1} and optical depths 10^5 , 10^6 and 10^7 . We see that the distribution is flat, meaning that the flux for all viewing angles is the same. The results for the central sources are similar.

3.2. Integrated Line Intensity

We consider possible variations in the integrated flux with respect to θ . We define the normalized flux seen by an observer at an angle μ by:

$$F(\mu) = \frac{2\Delta N}{N\Delta\mu}, \quad (4)$$

where $\mu = \cos \Theta$, N is the total number of outgoing photons, ΔN is the number of photons in an angular bin $\Delta\Theta$. This definition satisfies the condition $\int_{-1}^1 F(\mu) d\mu / 2 = 1$.

Figure 5 shows a flat $F(\mu)$ for all models. It means that in spite of the different morphologies, the integrated flux is the same for all sight angles.

3.3. Full Width at Half Maximum

We use the full width at half maximum (FWHM) to quantify the line broadening. We measure this width from the velocity histogram by finding the values of the velocities at half maximum. We use lineal interpolation between histogram points to get a more precise value for this width.

Figure 6 shows the FWHM for all models as a function of the viewing angle. The FWHM increases for decreasing values of μ increases and increasing values of V_{max} . In Figure ?? we fix $|\mu| < 0.1$ and show the FWHM as a function of rotational velocity. For this case we parametrize the dependency of the line width with V_{max} as

$$\text{FWHM}^2 = \text{FWHM}_0^2 + V_{\text{max}}^2 / \lambda^2, \quad (5)$$

where FWHM_0 is the velocity width in the static case and λ is a positive scalar to be determined as a fit to the data.

With this test we want to know to what extent the new velocity width can be expressed as a quadratic sum of the two relevant velocities in the problem. We fit simultaneously all the points corresponding to central and homogeneous models to find $\lambda_c = 0.84 \pm 0.06$ and $\lambda_h = 0.54 \pm 0.1$

Source Distribution	τ_H	V_{max} (km s^{-1})				
		0	50	100	200	300
Homogeneous	10^5	0.263	0.266	0.309	0.357	0.370
	10^6	0.289	0.289	0.309	0.360	0.393
	10^7	0.227	0.229	0.231	0.254	0.281
Central	10^5	0.096	0.097	0.096	0.096	0.096
	10^6	0.066	0.066	0.066	0.066	0.066
	10^7	0.015	0.016	0.016	0.016	0.015

TABLE 2
ESCAPE FRACTION VALUES FOR ALL DUSTY MODELS.

respectively.

3.4. Line Maxima

We measure the peak maxima position to quantify the transition from double into single peak. We do this as a function of the viewing angle θ and the maximum rotational velocity. The results are summarized in Figure 8. There are two interesting features that deserve attention. First, for a viewing angle parallel to the rotational axis ($\mu \sim 1.0$) the maxima of all models are similar regardless of the rotational velocity. Second, at a viewing angle perpendicular to the rotation axis ($\mu \sim 0.0$) there is a good fraction of models that become single peaked, a feature that appears more frequently for homogeneously distributed sources when all the other parameters are equal.

3.5. Dusty Clouds: Escape Fraction

We now estimate the escape fraction f_{esc} for the dusty models. Our main result is that we do not find any dependence with the viewing angle but there is a strong dependence with the rotational velocity for the homogeneous models.

The left panel in Figure 9 summarizes our results. The left panel shows the escape fraction as a function of the rotational velocity. To construct this Figure we take into account all the photons regardless of its outgoing direction. We observe that the curves for the central source distribution stay flat, while for the homogeneous case there is a clear rise with rotational velocity. Rotation has a higher relative impact in the models with low optical depth. For instance, in models with $\tau_H = 10^5$, the static escape fraction is 0.26 and increases to 0.37 for $V_{\text{max}} = 300 \text{ km s}^{-1}$. Table 2 lists all the values for the escape fraction.

In the right panel of Figure 9 we put these results in the context of the analytic solution for the infinite slab (Neufeld 1990). In Neufeld's set-up the analytic solution depends uniquely on the product $(a\tau_H)^{1/3}\tau_A$ where $\tau_A = (1 - A)\tau_a$, valid only in the limit $a\tau_H \gg 1$. The dashed lines in the right panel of Figure 9 show the results for the different rotational velocities for the homogeneous models. First of all we note that the escape fraction does not increase significantly from $\tau_H = 10^5$ to $\tau_H = 10^6$. This counter-intuitive result is a consequence of the transition into the 'extremely' opaque regime, which occurs roughly when $a\tau_H > 10^3$ e.g. (Neufeld 1990).

3.6. Average Number of Scatterings

The number of scatterings affects the escape frequency of a Ly α photon. Studying this quantity can help us

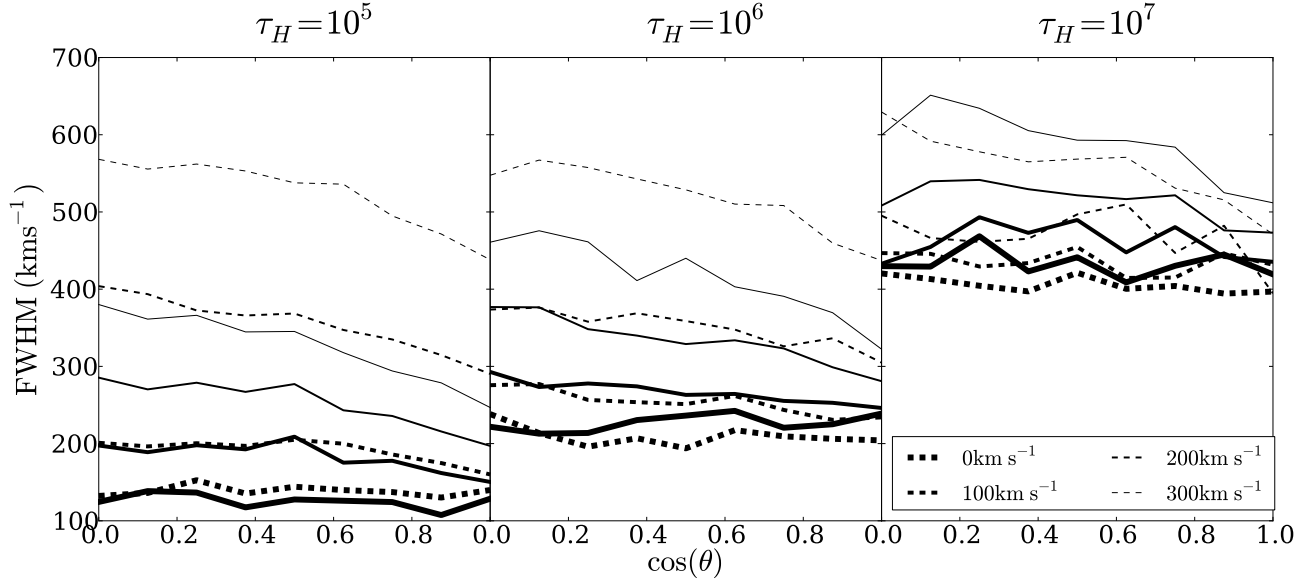


FIG. 6.— FWHM for the non-dusty models as a function of the viewing angle parameterized by $\mu \equiv \cos \theta$. Continuous (dashed) lines correspond to central (homogeneous) source distributions. The general trend is of an decreasing FWHM as the line of sight becomes parallel to the rotation axis.

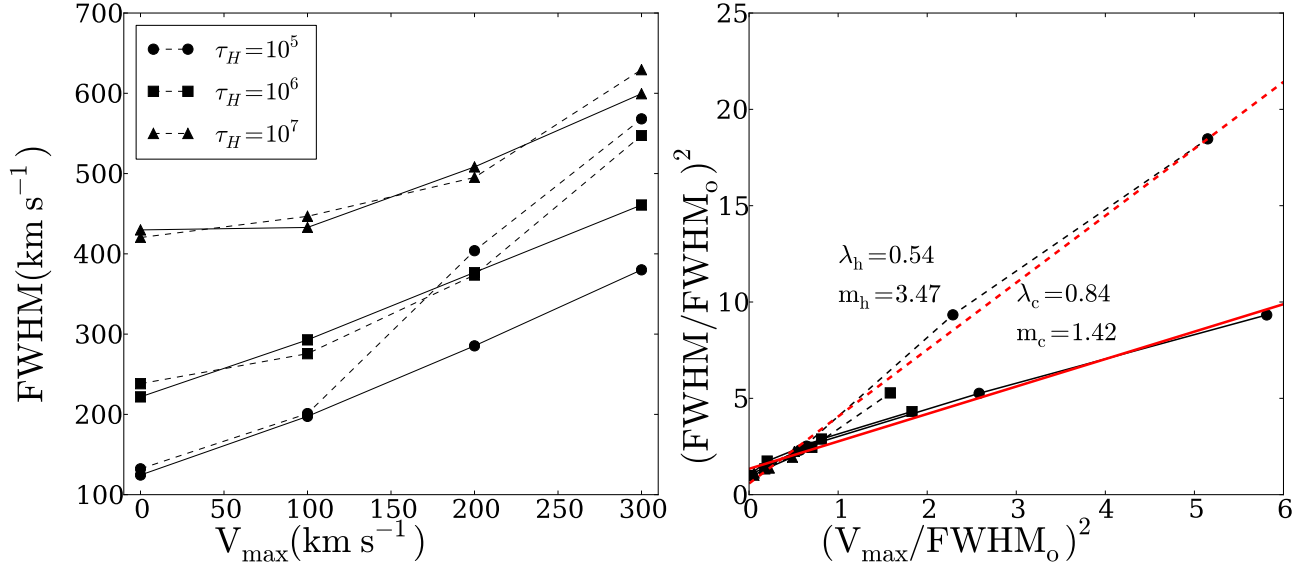


FIG. 7.— FWHM for the non-dusty models as a function of rotational velocity V_{\max} . The left panel shows the results in velocity units while the right panel normalizes the data by the FWHM in the static case. Continuous (dashed) lines correspond to central (homogeneous) source distributions. The straight lines represent the fit to the data using the expression in Eq. (5).

in clarifying two results that we have observed for homogeneous models in the previous sections: the quick emergence of a single peak and the increase in the escape fraction.

A possible explanation for these two results is that some photons close to the surface can escape with a low number of scatterings. This has a two-fold consequence: the escaping photons do not have time to scatter away from the line's center and also have less chances to find an absorbing dust grain.

In Figure 10 we show the average number of scatterings $\langle N_{\text{scatt}} \rangle$ as a function of the cosinus of the outgoing angle $|\cos \theta|$ and the rotational velocity V_{\max} . From the right

panel observe that the number of scatterings and the outgoing angle are independent. This plot corresponds to the specific case of the central model with $\tau = 10^5$ and $V_{\max} = 300 \text{ km s}^{-1}$; but we have verified that this holds for all models. This allows us to focus to use all the photons in the simulations regardless of their value of $\cos \theta$.

In the right panel of Figure 10 we observe how the average number of scatterings decreases for larger rotational velocities in the case of homogeneous source distributions. For instance, for $\tau_H = 10^5$ the average number of scatterings decreases by 61% at $V_{\max} = 300 \text{ km s}^{-1}$ in comparison to the static case. For the central source

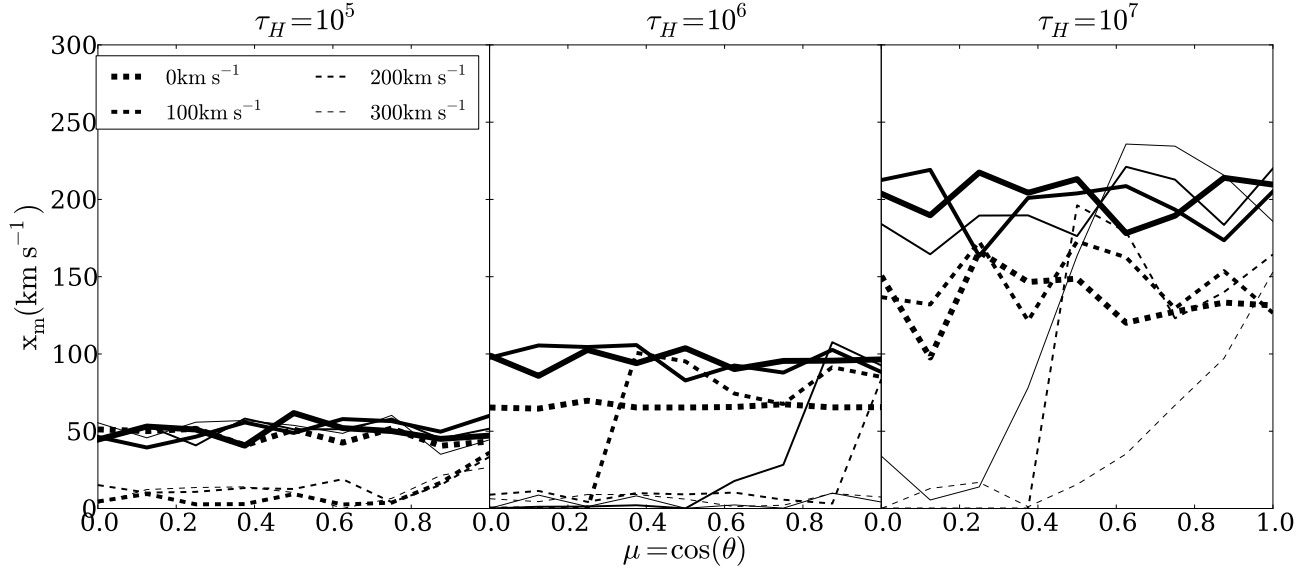


FIG. 8.— Position of the line maxima as a function of maximum rotational velocity V_{\max} . Continuous (dashed) lines correspond to central (homogeneous) source distributions. A value of $x_{\max} = 0$ indicates that line becomes single peaked.

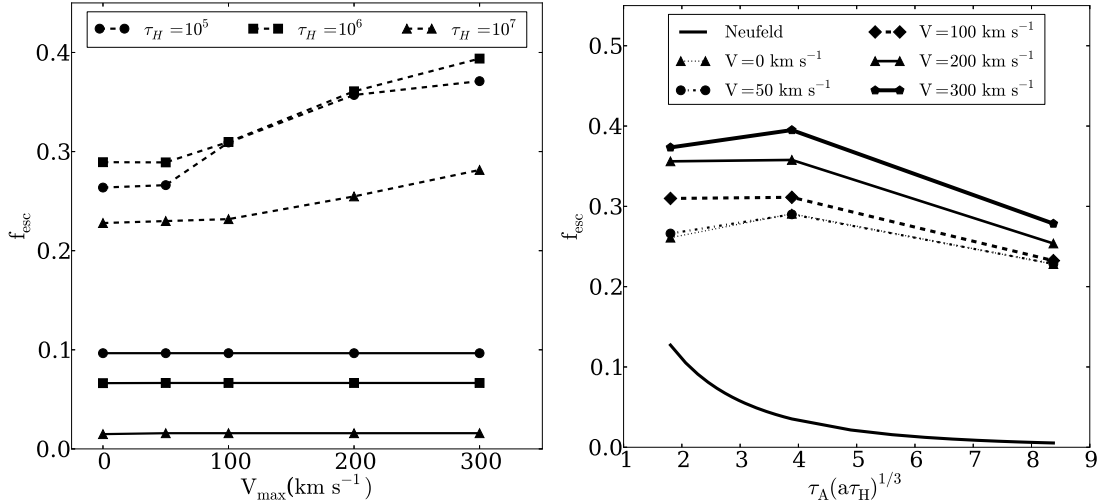


FIG. 9.— Effects of rotation on the escape fraction. Left panel, escape fraction as a function of rotational velocity. All these models have $\tau_a = 1$. The continuous (dashed) lines correspond to central (homogeneous) models. Right panel, escape fraction as a function of the product $(a\tau_H)^{1/3}\tau_A$. The analytic solution for the infinite slab is shown as a continuous line. Different lines correspond to different rotational velocities for the homogeneous models.

distribution the average number of scatterings $\langle N_{\text{scatt}} \rangle$ changes less than 0.5%.

In static cases, a large value of the optical depth correlates with a high number of scatterings. This can be precisely quantified in the static slab. In this model for centrally emitted sources the average number of scatterings depends only on the optical depth $\langle N_{\text{scatt}} \rangle = 1.612\tau_H$ (Adams 1972; Harrington 1973), in the case of homogeneously distributed sources $\langle N_{\text{scatt}} \rangle = 1.16\tau_H$ (Harrington 1973).

We perform a similar quantification of in our speherical setup for the static spheres. We find that for the central model the number of scatterings is proportional to the optical depth, with $\langle N_{\text{scatt}} \rangle = (1.50, 1.00, 0.92)\tau_H$ for optical depth values of $\tau_H = (10^5, 10^6, 10^7)$ respec-

tively. For the homogeneous static sphere we find that $\langle N_{\text{scatt}} \rangle = (0.99, 0.59, 0.51)\tau_H$, this represents factors of $(0.66, 0.59, 0.55)$ lower than the centrally emitted photons.

For the homogeneous rotating sphere at $V_{\max} = 300 \text{ km s}^{-1}$ we find that $\langle N_{\text{scatt}} \rangle = (0.38, 0.34, 0.42)\tau_H$ which represents factors of $(0.26, 0.34, 0.46)$ lower than the corresponding central case.

In order to gain a deeper understanding of these results we make 2D histograms for the number of scatterings as a function of the outgoing dimensionless frequency x . In Figure 11 we these results in the case $\tau_H = 10^5$ for the static case and $V_{\max} = 300 \text{ km s}^{-1}$. The upper (lower) panels show the results for the homogeneous (central) source distribution. The color scale is logarithmic in the

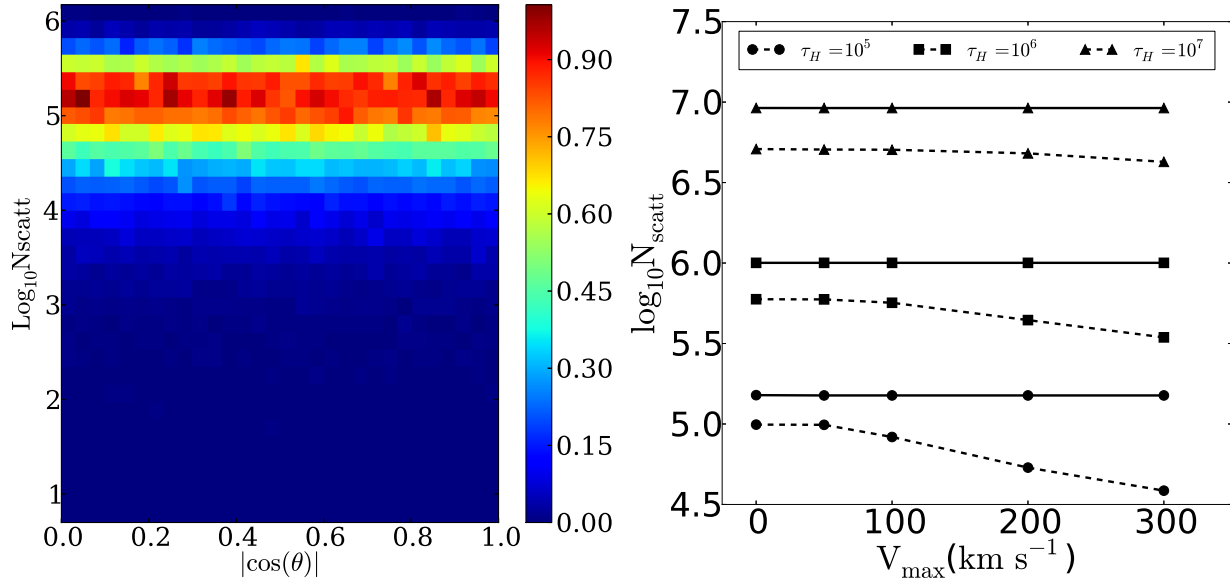


FIG. 10.— Logarithm of the average number of scatterings as function of μ (left panel) and the maximum rotational velocity V_{max} . The left panel shows the behaviour for $\tau = 10^5$ and $V_{\text{max}} = 300 \text{ km s}^{-1}$ but this independence of the independence between N_{scatt} and μ is kept for all models. In the right panel the continuous (dashed) lines represent an central (homogeneous) distribution of sources; this shows the clear decrease in the number of scatterings for the homogeneously distributed sources.

number of photons at a certain value $x - N_{\text{scatt}}$.

The top right panel of Figure 11 (homogeneous sources, high rotational velocity) supports our hypothesis about the photo-sphere in the homogeneous distribution. In this case most of the photons that left with $x \sim 0$ have escaped with less than 10 scatterings. This also explains the decrease in the average number of scatterings observed in Figure 10.

However, for a central distribution the situation is quite different (lower panels). In this case the number of scatterings remains high, in the order of the optical depth, but the two peaks do get closer to each other. Here the most probable physical picture is that each scattering, due to the bulk velocity of the gas, is inefficient in driving the photon outside the line center.

4. DISCUSSION

Gas bulk rotation has a noticeable effect on the morphology of the Ly α line. In this section we compare our findings to other computational results and discuss the implications of these finding in the interpretation of observational data.

Verhamme et al. (2012) studied Ly α using two high resolution simulations of individual galaxies. The main purpose of the study was to asses the impact of two different InterStellar Medium (ISM) prescriptions. However, each simulated galaxy had a disc structure with a clear rotation pattern in the ISM and inflowing gas into the circum-galactic region. The configuration had an axial symmetry and they reported a strong dependence of the escape fraction and the total line intensity as a function of the θ angle. In our results, none of these two quantities has a dependence either on the inclination angle or the rotational velocity. Therefore, the effect reported by Verhamme et al. (2012) is consistent with being a consequence of the different hydrogen optical depth for different viewing angles and not as an effect of the bulk rotation.

The presence of single peaked profiles has been associated to inflow/outflow dynamics (Verhamme et al. 2006; Dijkstra & Kramer 2012). In this paper we show that gas bulk rotation can also be considered as a probable origin for that behavior, provided that the observed single peak is highly symmetric. Similarly, in the case of double peaked lines with a high level of flux at the line center, rotation also deserves to be considered in the pool of possible bulk flows responsible for that feature, specially if the two peaks have similar intensities. This highlights that in order to interpret the observations of Ly α emitting galaxies it is necessary to consider the possible effect of different inclination angles along the line of sight.

5. CONCLUSIONS

This paper quantifies for the first time in the literature the effects of gas rotation in the morphology of the Ly α emission line in star forming galaxies. The results are based on the study of an homogeneous sphere of gas with solid body rotation. We explore a range of models by varying the rotational speed, hydrogen optical depth, dust optical depth and initial distribution of Ly α photons with respect to the gas density. As a cross-validation, we obtain our results from two independently developed Monte-Carlo radiative transfer codes.

Our main result is two-fold. First, rotation clearly impacts the Ly α line morphology. Second, rotation introduces an anisotropy for different viewing angles. For viewing angles close to the poles the line is double peaked and it makes a transition to a single peaked line for high rotational velocities and viewing angles along the equator. This trend is stronger for spheres with homogeneously distributed radiation sources. In contrast, the total flux in the line remains independent of the viewing angle.

The escape fraction remains constant for different viewing angles only in the case of centrally distributed sources. In contrast, for an homogeneous distribution the escape fraction decreases with high rotation frac-

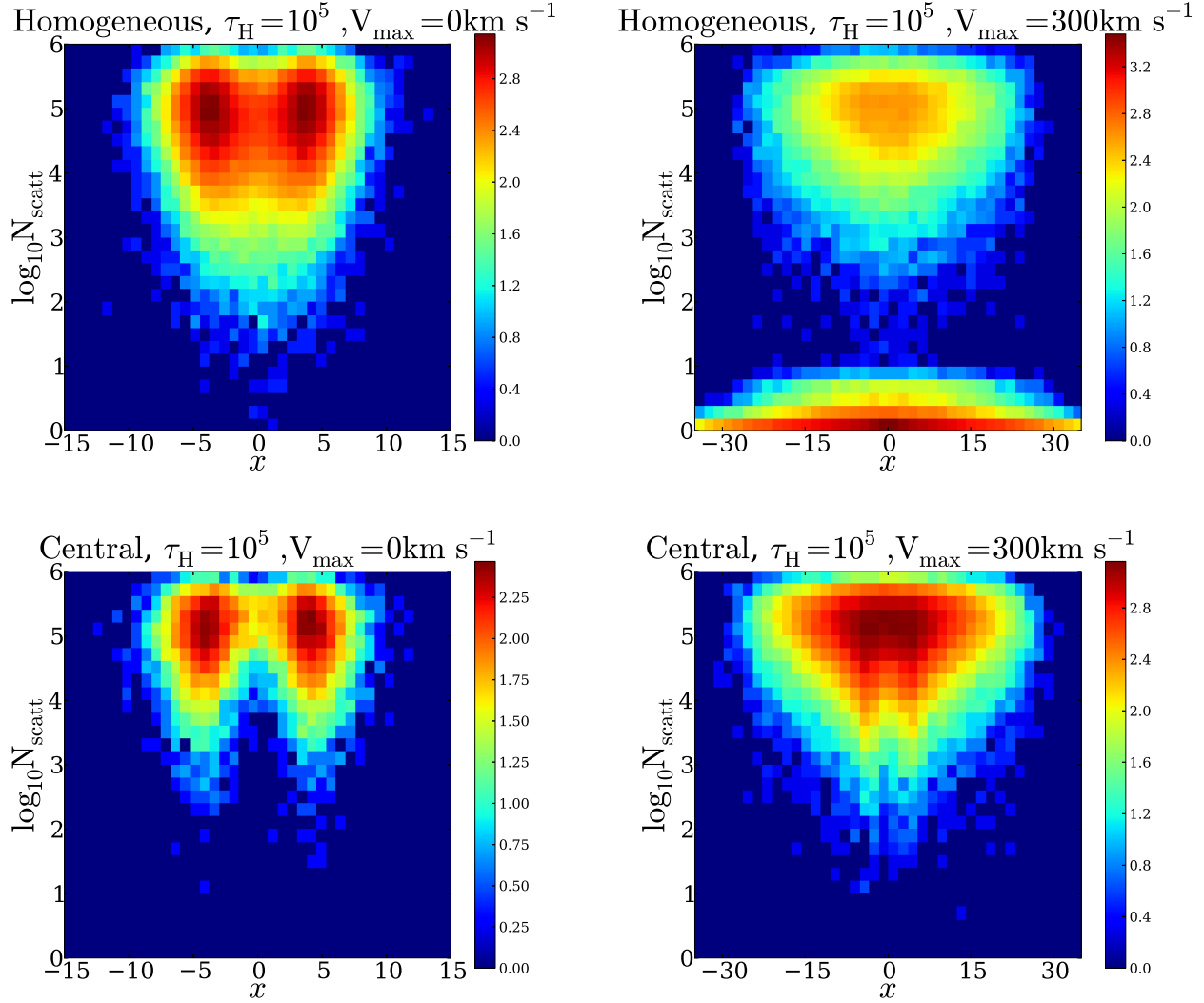


FIG. 11.— 2D histogram of N_{scatt} vs x . The upper (lower) panels show the homogeneous (central) source distribution. Left panels corresponds to the static case and right panels correspond to $V_{\text{max}} = 300 \text{ km s}^{-1}$. The color scale is logarithmic on the number of photons with given values of N_{scatt} and x .

tion remain constant for different viewing angles. We showed that these results can be interpreted in terms of the average number of scatterings for the photons, a quantity that also remains constant independent of the viewing angle and the rotational velocity for centrally distributed sources and decreases for homogeneously distributed source.

Quantitatively the main results of our study are summarized as follows.

- Rotation induces a considerable asymmetry in the morphology of the spectra when the viewing angle θ . This occurs for all of our models. The asymmetry is such that observed with $\cos \theta \equiv \mu \sim 1$, i.e. observers aligned with the rotation axis, the line is double peaked while for $\mu \sim 0$ and high rotation velocities the line becomes double peaked.
- For $\mu \sim 0$ The line width increases with rotational velocity. The line width approximately follows the functional for $\text{FWHM}^2 = \text{FWHM}_0^2 + (V_{\text{max}}/\lambda)^2$

where FWHM_0 indicates the line width for the static case and λ is a constant determined from the radiative transfer results it is $\lambda_c = 0.84 \pm 0.06$ and $\lambda_h = 0.54 \pm 0.10$ for the central and homogeneous source distribution, respectively.

- A single peaked line emerges for high rotational velocities in the case of homogeneously distributed sources. These cases occur when the rotational velocity is larger than half FWHM_0 and $\mu \sim 1$.
- For central sources we find that the escape fraction does not change with rotational velocity nor with the viewing angle. We interpret this in terms of the average number of scatterings which does not significantly changes with rotation. This is due to the fact that the vast majority of scatterings events are resonant, during which the mean free path is very short and the effect of gas bulk rotation is not enough to affect Ly α photons.

- For homogeneous sources we find that the as rotational velocity increases, the escape fraction rises by a factor of ~ 2 with respect to the static situation. We also interpret this change in terms of the average number of scatterings. In the second part of §3.3 we show that the average number of scatterings decreases a 40% compared to the static case, while a large fraction of photons escape with less than 10 scatterings.

Comparing our results with recent observed LAEs we find that many morphological features such as high central line flux, single peak profiles could be explained by gas bulk rotation present in these LAEs.

ACKNOWLEDGMENTS

JNGC acknowledges financial support from Universidad de los Andes.

JEFR acknowledges financial support from Vicerrectoria de Investigaciones at Universidad de los Andes through a FAPA grant.

We thank the International Summer School on AstroComputing 2012 organized by the University of California High-Performance AstroComputing Center (UC-HiPACC) for providing computational resources where some of the calculations were done.

The data, source code and instructions to replicate the results of this paper can be found here <https://github.com/jngaravitoc/RotationLyAlpha>. Most of our code benefits from the work of the IPython and Matplotlib communities (Pérez & Granger 2007; Hunter 2007).

REFERENCES

- Adams, T. F. 1972, *ApJ*, 174, 439
- Ahn, S.-H., Lee, H.-W., & Lee, H. M. 2000, *Journal of Korean Astronomical Society*, 33, 29
- . 2001, *ApJ*, 554, 604
- Ahn, S.-h., Lee, H.-w., & Lee, H. M. 2014, 000
- Auer, L. H. 1968, *ApJ*, 153, 783
- Avery, L. W., & House, L. L. 1968, *ApJ*, 152, 493
- Barnes, L. A., Haehnelt, M. G., Tescari, E., & Viel, M. 2011, *MNRAS*, 416, 1723
- Behrens, C., Dijkstra, M., & Niemeyer, J. C. 2014, *A&A*, 563, A77
- Behrens, C., & Niemeyer, J. 2013, *A&A*, 556, A5
- Dijkstra, M., Haiman, Z., & Spaans, M. 2006, *ApJ*, 649, 14
- Dijkstra, M., & Kramer, R. 2012, *MNRAS*, 424, 1672
- Finkelstein, S. L., Papovich, C., Dickinson, M., Song, M., Tilvi, V., Koekemoer, a. M., Finkelstein, K. D., Mobasher, B., Ferguson, H. C., Giavalisco, M., Reddy, N., Ashby, M. L. N., Dekel, a., Fazio, G. G., Fontana, a., Grogin, N. a., Huang, J.-S., Kocevski, D., Rafelski, M., Weiner, B. J., & Willner, S. P. 2013, *Nature*, 502, 524
- Forero-Romero, J. E., Yepes, G., Gottlöber, S., Knollmann, S. R., Cuesta, A. J., & Prada, F. 2011, *MNRAS*, 415, 3666
- Forero-Romero, J. E., Yepes, G., Gottlöber, S., & Prada, F. 2012, *MNRAS*, 419, 952
- Garel, T., Blaizot, J., Guiderdoni, B., Schaerer, D., Verhamme, A., & Hayes, M. 2012, *MNRAS*, 422, 310
- Gawiser, E., Francke, H., Lai, K., Schawinski, K., Gronwall, C., Ciardullo, R., Quadri, R., Orsi, A., Barrientos, L. F., Blanc, G. A., Fazio, G., & Feldmeier, J. J. 2007, *ApJ*, 671, 278
- Hansen, M., & Oh, S. P. 2006, *MNRAS*, 367, 979
- Harrington, J. P. 1973, *MNRAS*, 162, 43
- Hunter, J. D. 2007, *Computing In Science & Engineering*, 9, 90
- Koehler, R. S., Schuecker, P., & Gebhardt, K. 2007, *A&A*, 462, 7
- Laursen, P., Sommer-Larsen, J., & Andersen, A. C. 2009, *ApJ*, 704, 1640
- Loeb, A., & Rybicki, G. B. 1999, *ApJ*, 524, 527
- Neufeld, D. A. 1990, *ApJ*, 350, 216
- Orsi, A., Lacey, C. G., & Baugh, C. M. 2012, *MNRAS*, 425, 87
- Ouchi, M., Shimasaku, K., Akiyama, M., Simpson, C., Saito, T., Ueda, Y., Furusawa, H., Sekiguchi, K., Yamada, T., Kodama, T., Kashikawa, N., Okamura, S., Iye, M., Takata, T., Yoshida, M., & Yoshida, M. 2008, *ApJS*, 176, 301
- Partridge, R. B., & Peebles, P. J. E. 1967, *ApJ*, 147, 868
- Pérez, F., & Granger, B. E. 2007, *Computing in Science and Engineering*, 9, 21
- Rhoads, J. E., Malhotra, S., Dey, A., Stern, D., Spinrad, H., & Jannuzi, B. T. 2000, *ApJ*, 545, L85
- Schenker, M. A., Stark, D. P., Ellis, R. S., Robertson, B. E., Dunlop, J. S., McLure, R. J., Kneib, J.-P., & Richard, J. 2012, *ApJ*, 744, 179
- Verhamme, A., Dubois, Y., Blaizot, J., Garel, T., Bacon, R., Devriendt, J., Guiderdoni, B., & Slyz, A. 2012, *A&A*, 546, A111
- Verhamme, A., Schaerer, D., & Maselli, A. 2006, *A&A*, 460, 397
- Yajima, H., Li, Y., Zhu, Q., Abel, T., Gronwall, C., & Ciardullo, R. 2012, *ApJ*, 754, 118
- Yamada, T., Nakamura, Y., Matsuda, Y., Hayashino, T., Yamauchi, R., Morimoto, N., Kousai, K., & Umemura, M. 2012, *AJ*, 143, 79
- Zheng, Z., & Miralda-Escudé, J. 2002, *ApJ*, 578, 33
- Zheng, Z., & Wallace, J. 2013, *ArXiv e-prints*